Journal of
Applied Physics

RESEARCH ARTICLE | OCTOBER 05 2022

Photoexcited carrier dynamics in semi-insulating 4H-SiC by Raman spectroscopy

Meng-meng Gao; Liu-yan Fan; Xiao-ye Gong; Jing-lin You; Zhi-zhan Chen

J. Appl. Phys. 132, 135702 (2022)
https://doi.org/10.1063/5.0108903

AIP Publishing

Journal of
Applied Physics

ARTICLE

scitation.org/journal/jap

Photoexcited carrier dynamics in semi-insulating 4H-SiC by Raman spectroscopy

Cite as: J. Appl. Phys. **132**, 135702 (2022); doi: 10.1063/5.0108903
Submitted: 11 July 2022 · Accepted: 9 September 2022 ·
Published Online: 5 October 2022

View Online Export Citation CrossMark

Meng-meng Gao,[1] Liu-yan Fan,[1] Xiao-ye Gong,[2] Jing-lin You,[2] and Zhi-zhan Chen[1,a)]

AFFILIATIONS

[1] Department of Physics, Shanghai Normal University, 100 Guilin Road, Shanghai 200234, China
[2] State Key Laboratory of Advanced Special Steel and Shanghai Key Laboratory of Advanced Ferrometallurgy and School of Materials Science and Engineering, Shanghai University, 99 Shangda Road, Shanghai 200444, China

[a)] **Author to whom correspondence should be addressed:** zzchen@shnu.edu.cn

ABSTRACT

The photoexcited carrier dynamics of high-purity (HPSI) and vanadium-doped semi-insulating (VDSI) 4H-SiC irradiated by lasers with different wavelengths and powers were investigated. Raman spectra were measured at room temperature and the photoexcited carrier concentrations were extracted from the Raman line shape analysis of longitudinal optical phonon–plasmon coupled mode. It was found that the longitudinal optical (LO) peaks of HPSI and VDSI did not shift with laser power variations, due to a low concentration of photoexcited carriers, when a 532- nm laser was used. However, when a 355- nm laser was adapted, the relationship between the photoexcited carrier concentrations and the laser power was found to be nonlinear because of the dominance of trap-assisted Auger (TAA) recombination. The coefficient of TAA recombination was laser power–dependent. The proposed carrier dynamic model deepens the understanding of the physical mechanism of semi-insulating SiC irradiated by nanosecond laser and provides an insight into the interpretation of experimental phenomena related to laser energy in optoelectronic devices.

I. INTRODUCTION

Thanks to its excellent properties such as wide bandgap, high thermal conductivity, and high critical breakdown field strength, 4H-silicon carbide (4H-SiC) is one of the candidate materials for preparing electron devices with high temperature, high frequency, and high radiation resistance. The controllability of dopants on SiC conductivity extends its application areas, such as using intrinsic defects[1] or introducing vanadium (V) dopants[2] during crystal growth to compensate for excess shallow donor or shallow acceptor carriers to grow high-purity (HPSI)[3] and V-doped semi-insulating (VDSI) crystals.[4] So far, semi-insulating (SI) SiC has been considered as a candidate semiconductor material for high-voltage photoconductive switches.[5,6] Excess carrier recombination and diffusion of SI SiC irradiated by laser determines the electrical properties of the device. Therefore, proper attention must be paid to the photoexcited carrier dynamics of semi-insulating crystals during laser irradiation.

The carrier dynamics in 4H-SiC have been studied by various techniques, including time-resolved free carrier absorption,[7] microwave photoconductivity decay,[8] four-wave mixing technique,[9] and light-induced transient grating technique[10] and so on. Generally, the experimental data are fitted to the proposed physical model, incorporating the generation of photoexcited carriers, ambipolar diffusion, Shockley–Read–Hall (SRH) recombination, radiative recombination, and band–band Auger (BBA) recombination, to obtain the carrier lifetime or bipolar diffusion coefficient, assuming that SRH recombination is the dominant process affecting the bulk carrier lifetime. Unfortunately, this assumption is not always justified. As a matter of fact, the defect-assisted recombination mechanisms in semiconductors mainly involve either the SRH process or the trap-assisted Auger (TAA) recombination process.[11] As is known to all, SRH recombination is a two-step process whereby an electron (hole) is captured at the trap located at level E_t, and then a hole (electron) is captured. In this process, level E_t is referred to as a recombination center. TAA recombination involves two free electrons and one hole or two free holes and one electron. After an electron (hole) is captured at level E_t, subsequently, the excess energy is transferred to the other electron (hole), which is highly excited into its respective band.[12] Therefore, it is essential to carefully investigate which recombination mechanism plays an important role during laser irradiation of semi-insulating SiC.

Raman spectroscopy is a non-destructive method for characterization of materials. Raman scattering has always been an attractive subject, especially for the study of the structure and electronic properties of SiC. Due to strong bonding covalency, the Raman efficiency of SiC is high and the Raman signals are easily obtainable. The Raman parameters, such as intensity, width, peak frequency shift, and polarization of Raman bands, provide valuable information on crystal quality.[13,14] Raman measurements enable the detection of coupled modes of longitudinal optical (LO) phonon and plasma oscillation of free carriers whose spectral features depend on carrier concentration and carrier damping. Therefore, a great deal of attention has been paid to the analysis of longitudinal optical phonon–plasma coupled (LOPC) modes in SiC.[15] Klein *et al.* first calculated the free carrier concentration of 6H-SiC by LOPC mode with a 488- nm laser.[16] A Raman test was carried out with an extrinsic excitation wavelength (≥456.5 nm; i.e., the corresponding laser photon energy is less than the bandgap of 4H-SiC) and similar results were obtained for n-type SiC.[17–19] Temperature-dependent Raman spectra using a 532- nm laser for doped 4H-SiC with different concentrations were investigated and a linear relation between line shift and temperature was observed.[20,21] Raman measurements with a 325- nm laser were used to investigate the effect of the C/Si ratio and silicon substrate orientation on the free carrier concentration of epitaxial 3C-SiC films.[22] Liu *et al.* reported Raman scattering using a 325- nm laser of Al-implanted 4H-SiC. With increasing the laser power, the LOPC peak of the Al-implanted layer shows a red shift compared with that of the non-implanted one. However, no reasonable explanation or reliable proof for this phenomenon was put forward.[23]

Although the carrier dynamics of laser-irradiated SiC have been studied through different approaches in recent decades, the ***photoexcited*** carrier dynamics of laser-irradiated SI SiC is rarely investigated. In this contribution, the effects of laser wavelength and power on the LOPC mode of SI 4H-SiC were investigated systematically. We tried to elucidate the relationships among laser power, LOPC mode, and photoexcited carrier dynamics at different laser wavelengths. The results showed that trap-assisted Auger recombination determined the carrier concentrations with laser power, which was demonstrated by the LOPC modes from Raman spectra.

II. EXPERIMENTS

N-type and 350-μm-thick high-purity and vanadium-doped semi-insulating 4H-SiC wafers were cut into $1.5 \times 1.5\,\text{cm}^2$ and cleaned by the Radio Corporation of America (RCA) method. The Raman spectra were characterized by using a Raman spectrometer (Horiba Jobin-Yvon LabRAM HR800). Raman scattering measurements were performed at room temperature. A Nd:YAG laser was used as the excitation source. The laser beam was focused onto the sample surface by means of a microscope objective, which was also used to collect the scattered light. The laser parameters used in the test are listed in Table I. The spectra were obtained in a backscattering geometry, $z\ (x, -)\ z$, where z is parallel to the c axis of the crystal, and x is in the plane perpendicular to the c axis. The polarization of the scattered light was not analyzed. The used objective lens was a 20× objective. The numerical apertures of the objective lenses used in the Raman test for 532- and 355- nm laser irradiation were 0.28 and 0.4, respectively. According to the relationships among the laser wavelength (λ), the excitation spot diameter (d), and numerical aperture (NA), that is, $d = 1.22\lambda/\text{NA}$, the spot diameters on the sample surface for the 532- and 355- nm lasers were calculated to be 2.318 and 1.083 μm, respectively. The contribution to the Raman scattering of the regions out of focus was eliminated by using a confocal pinhole. The integration time and integration number in the Raman measurement were 10 s and 10, respectively. The Raman shift was calibrated by using a single-crystal Si wafer. Samples with the high-purity and vanadium-doped semi-insulating 4H-SiC were named HPSI-X and VDSI-X, respectively, where X referred to laser wavelength (i.e., 532 and 355 nm).

III. RESULTS AND DISCUSSION

The transverse optical (TO) and longitudinal optical (LO) modes of HPSI and VDSI vs laser powers under 532- nm laser irradiation are exhibited in Fig. 1. The Raman shifts of the TO and LO modes do not vary with laser powers. The former is 777.32 cm^{-1}, which is similar to that reported by Ref. 24, while the latter is 964.35 cm^{-1}, which represents the ideal position of an unintentionally doped 4H-SiC.

The Raman modes of HPSI and VDSI by the 355- nm laser irradiation are displayed in Fig. 2. Like the 532- nm laser irradiation, the Raman peaks of the TO mode for HPSI-355 and VDSI-355 are also located at 777.32 cm^{-1}, which are independent of laser power as shown in Fig. 2(c). The difference appears in the LO mode. Generally speaking, as shown in Fig. 2(d), with an increase in laser power, the ω_{LOPC} of both HPSI and VDSI first increases linearly, then deviates from linear relation, and finally tends to saturation. Furthermore, the ω_{LOPC} of VDSI is less than that of HPSI and achieve saturation in advance. Specifically, in the case of HPSI-355, the LO modes are centered at 964.35 cm^{-1}, which is the same as that of HPSI-532, when the laser powers are 0.003 and 0.03 mW; by increasing the laser power to 0.3 mW, the position of the LO mode moves to 964.64 cm^{-1} and is defined as the LOPC mode. Upon further increasing, the laser power from 0.96 to 1.5 mW and then to 1.95 mW and the positions shift from

TABLE I. Parameters in the Raman measurement.

λ (nm)	Repetition frequency (kHz)	Pulse width (ns)	Laser power (mW)	Numerical aperture (NA)	Spot diameter (μm)
532	10	34	0.011–11	0.28	2.318
355	10	20	0.003–41	0.4	1.083

964.92 to 965.50 cm^{-1} and then to 966.62 cm^{-1}. When the laser power is increased to 41 mW, the center position of LOPC shifts to 970.32 cm^{-1}. Unlike HPSI-355, the positions of the LO mode of VDSI-355 maintain at 964.35 cm^{-1} until the power is 1.5 mW, which is connected to the lifetime of carriers. They shift toward the higher-frequency side at a higher laser power; for example, it is 965.38 cm^{-1} at 1.95 mW and 965.85 cm^{-1} at 41 mW. Compared from Figs. 2(a2) and 2(b2), the obvious difference is that the LOPC modes for HPSI-355 gradually broaden and become asymmetric as the laser powers increase, while they remain symmetrical for VDSI-355.

The carrier concentration (n) of SiC can be extracted from the Raman line shape analysis of the LOPC mode. Theoretical fitting is established in the framework of a dielectric model by Hon and Faust,[25] Klein,[26] and Irmer *et al.*[27] The Raman intensity of the LOPC mode can be written by

$$I(\omega) = SA(\omega)\mathrm{Im}\left[-\frac{1}{\varepsilon(\omega)}\right], \tag{1}$$

where ω is the Raman shift, S is a proportionality constant, $\varepsilon(\omega)$ is the dielectric function, and $A(\omega)$ is given by the following expression:[27–29]

$$A(\omega) = 1 + \frac{2C\omega_{TO}^2\left[\omega_p^2\gamma(\omega_{TO}^2-\omega^2)-\omega^2\Gamma(\omega^2+\gamma^2-\omega_p^2)\right]}{\Delta} + \frac{(C^2\omega_{TO}^4/\Delta)\left\{\omega_p^2\left[\gamma(\omega_{LO}^2-\omega_{TO}^2)+\Gamma(\omega_p^2-2\omega^2)\right]+\omega^2\Gamma(\omega^2+\gamma^2)\right\}}{\omega_{LO}^2-\omega_{TO}^2}, \tag{2}$$

$$\Delta = \omega_p^2\gamma\left[(\omega_{TO}^2-\omega^2)^2+(\omega\Gamma)^2\right]+\omega^2\Gamma(\omega_{LO}^2-\omega_{TO}^2)(\omega^2+\gamma^2), \tag{3}$$

where ω_{TO} and ω_{LO} are the uncoupled TO- and LO-phonon frequencies, ω_{p} is the plasma frequency that is related to n, γ is the plasmon damping constant, Γ is the phonon damping constant, and C is the so-called Faust–Henry coefficient, which is related to the ratio of the Raman intensity of the LO phonon mode to that of the TO phonon mode in the pure SiC crystal. The dielectric function $\varepsilon(\omega)$ is given by contributions from phonons and plasmas,

$$\varepsilon(\omega) = \varepsilon_\infty\left[1+\frac{\omega_{LO}^2-\omega_{TO}^2}{\omega_{TO}^2-\omega^2-i\omega\Gamma}-\frac{\omega_p^2}{\omega(\omega+i\gamma)}\right], \tag{4}$$

where ε_∞ is the high frequency dielectric constant.

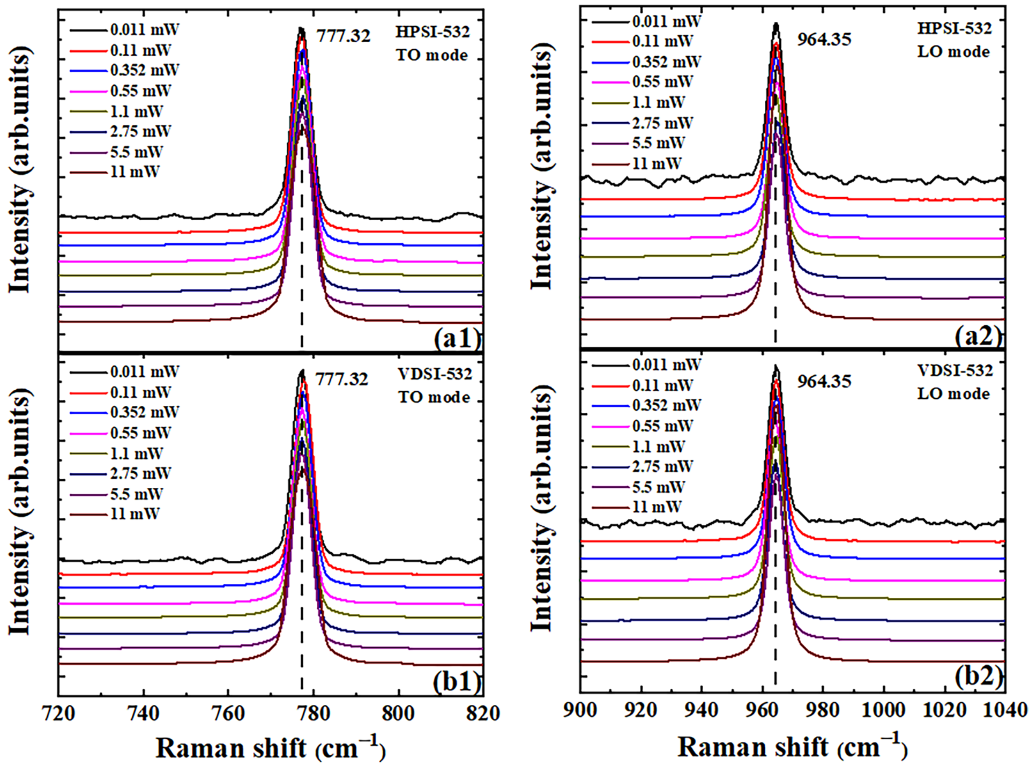

FIG. 1. Raman modes of HPSI-532 (a) and VDSI-532 (b) for average laser powers at 300 K. (a1) and (b1) TO modes; (a2) and (b2) LO modes.

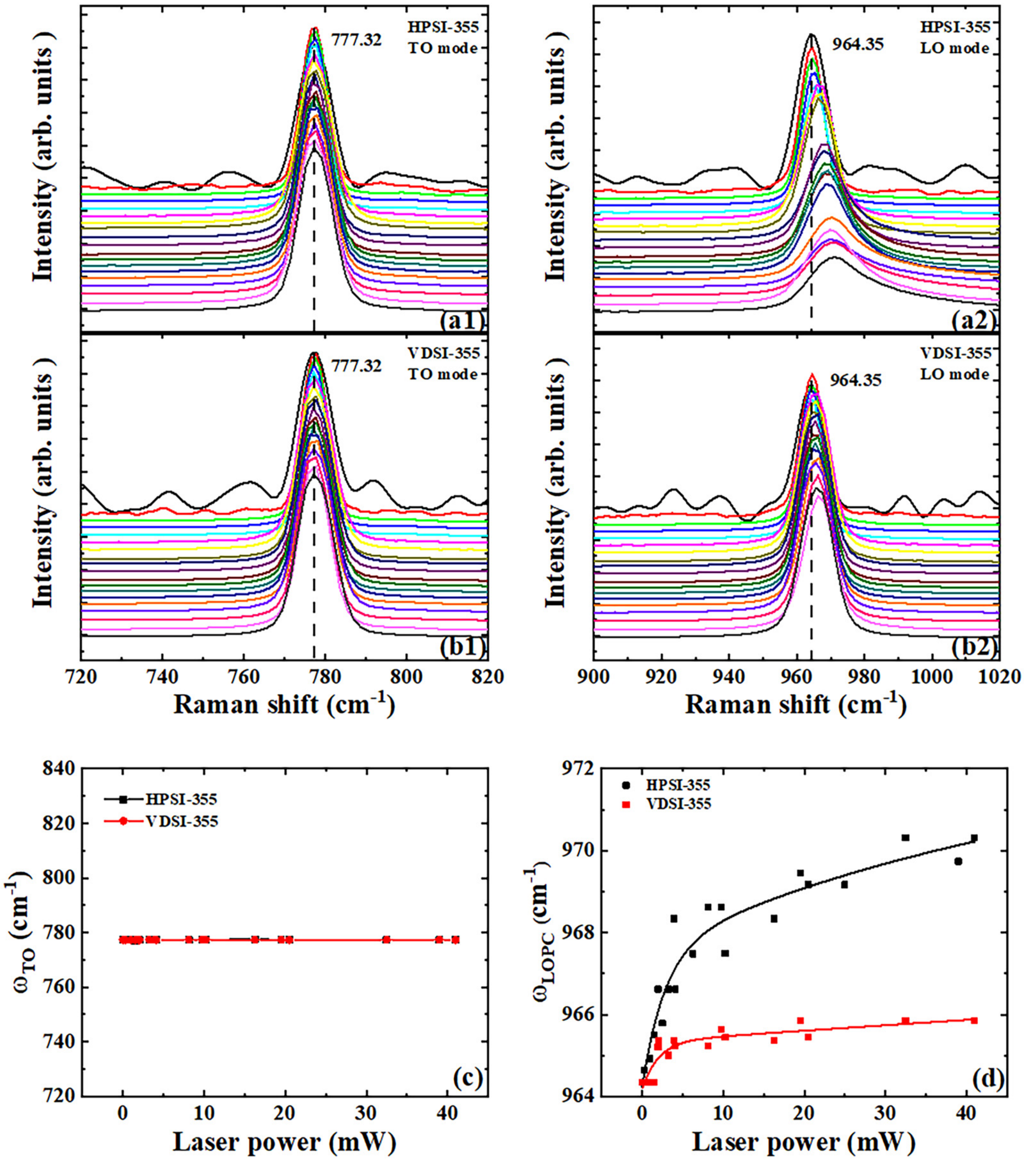

FIG. 2. Raman modes and their frequencies of HPSI-355 (a) and VDSI-355 (b) for different laser powers at 300 K. (a1) and (b1) TO mode; (a2) and (b2) LO/LOPC mode; (c) ω_{TO}; (d) ω_{LOPC}. Black, red, green, blue, cyan, magenta, yellow, dark yellow, navy, purple, wine, olive, dark cyan, royal, orange, violet, pink, LT magenta, and park gray lines in (a) and (b) refer to 0.003, 0.03, 0.3, 0.96, 1.5, 1.95, 2.05, 3.25, 3.9, 4.1, 8.12, 9.75, 10.25, 16.25, 19.5, 20.5, 32.5, 39, and 41 mW, respectively.

TABLE II. Parameters used to fit experimental Raman spectra by using Eqs. (1)–(4).

Parameters	Comment	Value
m^*	Effect mass	0.48 m_0
ω_{TO}	TO phonon frequency	777.32 cm^{-1}
ω_{LO}	LO phonon frequency	964.35 cm^{-1}
ε_∞	High-frequency dielectric constant	6.51

The mathematical analysis software MATLAB is adopted to fit Eqs. (1)–(4) to observe the LOPC mode profiles in our experiment using Γ, γ, ω_p, and C as adjustable parameters. Their numerical values are obtained by using the MATLAB fitting procedure. The electron effective mass (m^*) is taken from Ref. 30. As ω_{LO} is the uncoupled LO-phonon frequency, it can be obtained from the undoped or low doped ($<10^{16}$ cm^{-3}) SiC.[31] In this contribution, ω_{LO} and ω_{TO} are determined from the Raman spectra of HPSI-355 at 0.03 mW. Based on the Lyddane–Sachs–Teller (LST) relation,[32]

$$\frac{\omega_{LO}^2}{\omega_{TO}^2} = \frac{\varepsilon_s}{\varepsilon_\infty}, \tag{5}$$

where ε_s is the static dielectric constant. The value of ε_∞ at 355 nm can be calculated to be 6.51. The parameters used in the fitting process are listed in Table II.

Once the parameters ω_p were obtained, the value of n of SiC was calculated by using the following equation:

$$n = \frac{4\pi^2 \varepsilon_0 \varepsilon_\infty \omega_p^2}{q^2} \times 10^{-6}. \tag{6}$$

According to Eqs. (1)–(6), ω_p and n of HPSI-355 and VDSI-355 vs laser power are shown in Fig. 3. In the case of HPSI-355, as shown in Figs. 3(a1) and 3(a2), ω_p and n linearly increase from 65 to 130 cm^{-1} and 1.47×10^{17} to 4.22×10^{17} cm^{-3}, respectively, when the laser power increases in the range of 0.3–1.95 mW, while they increase nonlinearly in a relatively high-power range (1.95–19.5 mW). When the power is more than 19.5 mW, they gently augment and gradually reach the saturation values of 290 cm^{-1} and 1.49×10^{18} cm^{-3} (41 mW). Such high photoexcited carrier concentrations explain the phenomenon that the LOPC modes of HPSI-355 are asymmetrically broadened and frequency shifted at high laser powers. This is due to the coupling between phonons and a large number of plasmons. Due to no coupling between LO phonon and plasma in the range of 0.3–1.5 mW (ω_{LO} is 964.35 cm^{-1}) for VDSI-355, we only consider the coupling phenomenon with a power greater than 1.5 mW as shown in Figs. 3(b1) and 3(b2). When the power is at 1.95 mW, they are severally 80 cm^{-1} and 2.23×10^{17} cm^{-3}. They increase nonlinearly and marginally with increasing laser power. They can only go up to 92 cm^{-1} and 2.95×10^{17} cm^{-3}, respectively, at 41 mW. Obviously, the LOPC modes maintain their symmetry for VDSI-355 due to the low photoexcited carrier concentration.

In order to account for the above phenomena, the carrier dynamics of HPSI and VDSI by 355 and 532 nm laser irradiation are investigated. The schematic energy level diagrams of HPSI and VDSI are shown in Fig. 4. As shown in Fig. 4(a), the HPSI substrate is assumed to exist in six defect centers, namely, a $Z_{1/2}$ recombination center (RC), a deep electron trap that is related to carbon vacancy (ET), a deep hole trap (HT), two kinds of nitrogen-related shallow donors, and a boron-related shallow acceptor (SA).[33] Two shallow donors (SD) are associated with the occurrence of nitrogen atoms, which replace carbon atoms present in the hexagonal (*h*) and cubic (*k*) sites of the 4H-SiC crystal lattice and are severally defined as SD1 and SD2.[34] Besides SD1, SD2, and SA, vanadium (V) impurities act as acceptors and are introduced to compensate for excess nitrogen donors, giving rise to the insulating state of SiC in the dark as shown in Fig. 4(b) for the VDSI substrate. It is hypothesized that an electron trap midgap level (ETM) represents all trap levels filled with electrons and a single electron trap level (ET1) is used to denote traps located within one $k_B T$ (k_B is Boltzmann constant) below the vanadium acceptor level. The above energy level positions are listed in Table III.

When irradiating the sample with a 532- nm laser, the energy is equivalent to 2.332 eV, which is less than the bandgap of 4H-SiC (3.26 eV). We can anticipate that the electrons on the ET, RC, SD1, and SD2 energy levels undergo transitions by absorbing photon energy, and electrons in the conduction band are also captured. Thus, supposing that the electron concentration in the conduction band at a certain time of laser irradiation is N, ignoring the intrinsic electron concentration N_i in the conduction band at equilibrium state and thermal excitation effect, the variation of N with time (t) is given by

$$\begin{aligned}\frac{dN}{dt} = {} & K\sigma_{opET} I(t)(N_{ET0} - N) + K\sigma_{opRC} I(t)(N_{RC0} - N) + K\sigma_{opSD1} I(t)(N_{SD10} - N) + K\sigma_{opSD2} I(t)(N_{SD20} - N) \\ & - \sigma_{nRC} v_{th} N \left[\begin{array}{c} (N_{RC} - N_{RC0}) + \dfrac{\sigma_{nET}}{\sigma_{nRC}}(N_{ET} - N_{ET0}) \\ + \dfrac{\sigma_{nSD1}}{\sigma_{nRC}}(N_{SD1} - N_{SD10}) + \dfrac{\sigma_{nSD2}}{\sigma_{nRC}}(N_{SD2} - N_{SD10}) + N \end{array} \right],\end{aligned} \tag{7}$$

$$K = \frac{\eta(1 - R)\exp(-\alpha W)}{\pi\left(\dfrac{d}{2}\right)^2 W\hbar\omega}, \tag{8}$$

$$I(t) = \frac{P}{t_p \cdot f}\exp\left[-4\ln 2\,\frac{(t - t_0)^2}{t_p^2}\right], \tag{9}$$

where σ_{opY}, σ_{nY}, N_Y, and N_{Y0} are the optical transition cross section, electron capture cross section, density of Y, and density of Y occupied by electrons; Y is referred to as ET, RC, SD1, and SD2, respectively; η is the quantum efficiency; R is the reflectance; α is the absorption coefficient; v_{th} is the electron thermal velocity; W is the thickness of the sample; d is the laser spot diameter; $\hbar\omega$ is the phonon energy; P is the average laser power; f is the repetition frequency; and t_p is the pulse width of the laser that is centered around $t_0 = 100$ ns. The parameters involved in the calculation are tabulated in Table IV.

When the 532- nm laser irradiates VDSI, the photon energy is just above the threshold energy of electron transition from ET1, VA, and ETM, and thus, electrons at these three levels can achieve optical transition to the conduction band, but electrons captured at other levels deeper in the 4H-SiC bandgap do not undergo optical transition. Under this circumstance, variation of N for VDSI as a function of time is expressed by

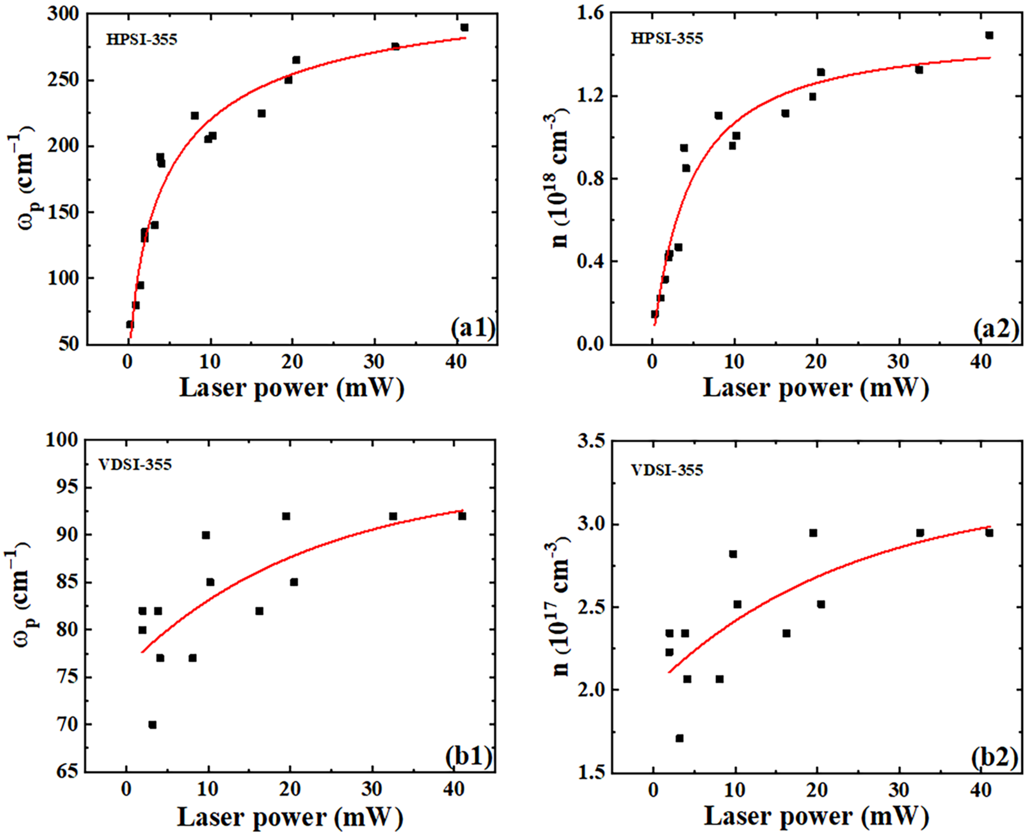

FIG. 3. ω_p and n with average laser powers. (a1) and (a2) HPSI-355; (b1) and (b2) VDSI-355.

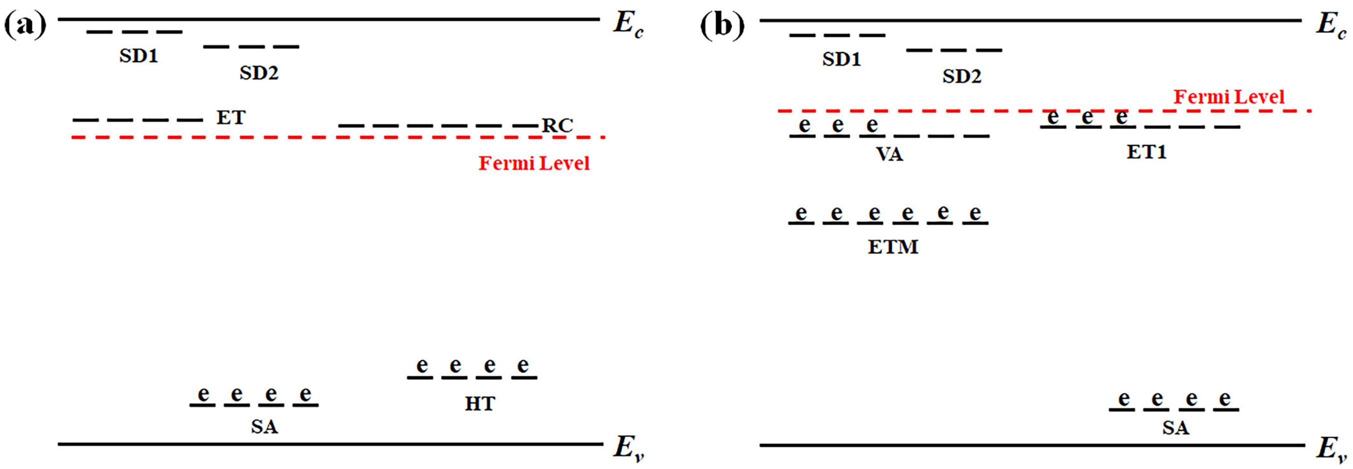

FIG. 4. Schematic energy level diagrams of HPSI (a) and VDSI (b).

$$\frac{dN}{dt} = K\sigma_{opETM}I(t)(N_{ETM} - N) + K\sigma_{opET1}I(t)(N_{ET10} - N) + K\sigma_{opVA}I(t)(N_{VA0} - N) - \sigma_{nET1}v_{th}N\left[(N_{ET1} - N_{ET10}) + \frac{\sigma_{nVA}}{\sigma_{nET1}}(N_{VA} - N_{VA0}) + N\right], \tag{10}$$

where σ_{opZ}, σ_{nZ}, N_Z, and N_{Z0} are the optical transition cross section, electron capture cross section, density of Z, and density of Z occupied by electrons, and Z is referred to as ETM, ET1, and VA, respectively. The above parameters are listed in Table V.

Numerical calculations by MATLAB are made according to Eqs. (7)–(10), and the carrier concentration distributions of HPSI-532 and VDSI-532 as a function of time at different laser powers are displayed in Fig. 5. In the range of 0.0011–11 mW, the N of HPSI-532 has a maximum value of $9.0 \times 10^{13}\,\mathrm{cm}^{-3}$ ($t = 100$ ns) [Fig. 5(a)]. However, it is much less than the minimum free carrier concentration ($2 \times 10^{16}\,\mathrm{cm}^{-3}$) determined by Raman spectroscopy using LOPC modes,[31] which is consistent with corresponding Raman results [Fig. 1(a2)]. At the laser power of 0.0011–0.352 mW, the maximum values of N ($N_{\max}$) for VDSI-532 increase from 5.76×10^{15} to $1.98 \times 10^{16}\,\mathrm{cm}^{-3}$ ($t = 100$ ns), which is also less than this limitation. However, as the laser power increases, $N_{\max}$ adds to $2.80 \times 10^{16}\,\mathrm{cm}^{-3}$ at 11 mW. Although $N_{\max}$ is larger than the limitation when the laser power is higher than 0.352 mW, it is difficult to observe an LOPC peak due to low Raman sensitivity.

In view of the fact that the photon energy (3.495 eV) of the 355- nm laser is larger than the 4H-SiC bandgap, not only can the electrons on the defect level in the bandgap transit, but also electrons in the valence band absorb the energy of the incident photons and transit into the conduction band, forming electron–hole pairs simultaneously. In constructing a physical model for SiC irradiated by the 355- nm laser during Raman measurement, we have made the following assumptions: (1) All trap levels in the bandgap are represented by a trap level with the density of N_T and the Shockley–Read–Hall (SRH) recombination lifetime of t_{SRH}. (2) Typical physical parameters of SiC are temperature-dependent. (3) The electron temperature is equal to the lattice temperature, which is due to the fact that the laser pulse width (20 ns) is greater than the carrier–phonon coupling time (0.1–10 ps).[45] (4) The surface recombination is ignored. (5) Since SiC is the indirect semiconductor, radiation recombination is ignored. As the diameter of the laser spot of 1.083 μm is much less than the penetration depth of 54.8 μm, the problem is two-dimensional. Based on the above hypotheses, the coupled diffusion equations for carrier concentration (N) and lattice temperature (T) can be written as[46]

TABLE III. Positions of energy levels in HPSI and VDSI 4H-SiC substrates.

Label	Comment	Energy position (eV)	Reference
SD1	SD in h site	$E_c - 0.05$	34
SD2	SD in k site	$E_c - 0.092$	34
ET	Electron trap	$E_c - 0.55$	36
RC	$Z_{1/2}$ recombination center	$E_c - 0.63$	37
HT	Hole trap	$E_v + 1.125$	38
SA	Boron-related shallow acceptor	$E_v + 0.285$	39
VA	Vanadium deep acceptor	$E_c - 0.8$	40
ETM	Electron trap mMidgap	$E_c - 1.6$	41
ET1	Electron trap 1	$E_c - 0.79$	41

$$\frac{dN}{dt} = D'\left[\nabla^2 N + \frac{N}{2k_B T}\nabla^2 E_g(T) + \frac{N}{2T}\nabla^2 T\right] + \frac{\eta I(t)(1-R)\alpha\exp(-\alpha z)}{\hbar\omega} - \frac{N}{t_{SRH}} - C_{TA}N_T N^2 - \gamma_0 N^3, \tag{11}$$

$$\frac{dT}{dt} = D_L\nabla^2 T + \frac{\eta I(t)(1-R)\alpha\exp(-\alpha z)}{C}\left[\frac{\hbar\omega - E_g(T) - 3k_B T}{\hbar\omega}\right] + \frac{\gamma_0 N^3}{C}[E_g(T) + 3k_B T]. \tag{12}$$

For the sake of the convenience of calculation, Cartesian coordinates are converted to cylindrical coordinates, and we have

$$\frac{dN}{dt} = D'\left\{\frac{1}{r}\frac{\partial}{\partial}\left(r\frac{\partial N}{\partial r}\right) + \frac{N}{2T}\left(1 + k_B^{-1}\frac{\partial E_g(T)}{\partial T}\right)\frac{1}{r}\frac{\partial}{\partial}\left(r\frac{\partial T}{\partial r}\right)\right\} + \frac{\eta I(t)(1-R)\alpha\exp(-\alpha z)}{\hbar\omega} - \frac{N}{t_{SRH}} - C_{TA}N_T N^2 - \gamma_0 N^3, \tag{13}$$

$$\frac{dT}{dt} = D_L\left[\frac{1}{r}\frac{\partial}{\partial}\left(r\frac{\partial T}{\partial r}\right)\right] + \frac{\eta I(t)(1-R)\alpha\exp(-\alpha z)}{C}\left[\frac{\hbar\omega - E_g(T) - 3k_B T}{\hbar\omega}\right] + \frac{\gamma_0 N^3}{C}[E_g(T) + 3k_B T], \tag{14}$$

where D' is the ambipolar diffusivity, E_g is the bandgap, z is the penetration depth, t_{SRH} is the nonradiative trap-related SRH lifetime, N_T is the density of the trap, C_{TA} is the trap-assisted Auger recombination (TAA) coefficient,[47] γ_0 is the band–band Auger recombination (BBA) coefficient, D_L is the 1attice thermal diffusivity, and C is the specific heat. Equation (13) gives the evolution of carrier concentration in virtue of the equation of continuity. The first term on the right is the photoexcited carrier current density on account of ambipolar diffusion, the second one

TABLE IV. Important parameters of HPSI-532 used in Eqs. (7)–(9).

Parameters	Comment	Value	Reference
σ_{opET}	Carbon vacancy optical transition cross section	1.2×10^{-15} cm^2	42
σ_{opRC}	$Z_{1/2}$ center optical transition cross section	1.3×10^{-14} cm^2	37
σ_{opSD1}	N donor in the hexagonal (*h*) site optical transition cross section	4.0×10^{-20} cm^2	35
σ_{opSD2}	N donor in the cubic (*k*) site optical transition cross section	4.0×10^{-19} cm^2	35
N_{ET}	Carbon vacancy density	5.0×10^{14} cm^{-3}	
N_{ET0}	Density of carbon vacancy occupied by an electron	3.73×10^{12} cm^{-3}	
N_{RC0}	Density of the $Z_{1/2}$ center level occupied by an electron	9.63×10^{13} cm^{-3}	
N_{RC}	$Z_{1/2}$ center density	8×10^{14} cm^{-3}	
N_{SD1}	Density of the N donor in the *h* site	5×10^{15} cm^{-3}	
N_{SD10}	Density of the N donor in the *h* site level occupied by an electron	1.23×10^{5} cm^{-3}	
N_{SD2}	Density of the N donor in the *k* site	5×10^{15} cm^{-3}	
N_{SD20}	Density of the N donor in the *k* site level occupied by an electron	6.26×10^{5} cm^{-3}	
σ_{nRC}	$Z_{1/2}$ center electron capture cross section	1.3×10^{-14} cm^2	43
σ_{nET}	Carbon vacancy electron capture cross section	1.2×10^{-15} cm^2	42
σ_{nSD1}	N donor in the *h* site electron capture cross section	4×10^{-20} cm^2	35
σ_{nSD2}	N donor in the *k* site electron capture cross section	4×10^{-19} cm^2	35
η	Quantum efficiency	1	
R	Reflectance	0.225	
α (at 532 nm)	Optical absorption coefficient	2 cm^{-1}	
d	Spot diameter	2.318×10^{-4} cm	
W	Thickness	0.035 cm	
t_p	Pulse width	34 ns	
v_{th}	Electron thermal velocity	1.17×10^{7} cm/s	
$\hbar\omega$	Photon energy	2.332 eV	

dotes the generation rate of the photogenerated carrier due to absorption of photons by the substrate, and others refer to SRH, TAA, and BBA recombination, respectively. Equation (14) is the thermal diffusion equation. The first term on the right represents the thermal diffusion, and the second and third ones refer to the sources of lattice heating associated with intrinsic absorption and Auger recombination, respectively.

The initial conditions are given by

$$\begin{aligned} N(r, 0) &= N_i, \\ T(r, 0) &= 300\ \text{K}, \end{aligned} \tag{15}$$

and the boundary conditions are as follows:

$$\left.\frac{\partial N}{\partial r}\right|_{r=0} = \left.\frac{\partial N}{\partial r}\right|_{r=r_0} = \left.\frac{\partial T}{\partial r}\right|_{r=0} = \left.\frac{\partial T}{\partial r}\right|_{r=r_0} = 0, \tag{16}$$

where N_i is the intrinsic carrier concentration. The above parameters involved in the calculation are listed in Table VI.

The simulation results are shown in Figs. 6(a) and 6(b). Attention is paid to the peak of N. It occurs at about $t = t_0$. As the laser power increases, $N_{\max}$ of HPSI-355 increases from 4.75×10^{17} to 4.52×10^{18} cm^{-3}. Unlike HPSI-355, there is no positive correlation between $N_{\max}$ and laser power for VDSI-355, suggesting that

TABLE V. Important parameters of VDSI-532 used in Eqs. (8)–(10).

Parameters	Comment	Value	Reference
σ_{opTM}	Electron trap midgap optical transition cross section	1×10^{-17} cm^2	41
σ_{opET1}	Electron trap 1 optical transition cross section	1×10^{-17} cm^2	41
σ_{opVA}	Vanadium acceptor level optical transition cross section	1×10^{-17} cm^2	41
N_{TM}	Electron trap midgap density	1.5×10^{16} cm^{-3}	
N_{T10}	Density of electron trap 1 occupied by an electron	2.5×10^{15} cm^{-3}	
N_{Va0}	Density of vanadium acceptor level occupied by an electron	6.49×10^{16} cm^{-3}	
N_{ET1}	Electron trap 1 density	5×10^{15} cm^{-3}	41
N_{VA}	Vanadium acceptor density	1.3×10^{17} cm^{-3}	
σ_{nET1}	Electron trap 1 electron capture cross section	7.9×10^{-14} cm^2	41
σ_{nVA}	Vanadium acceptor electron capture cross section	5.77×10^{-16} cm^2	44

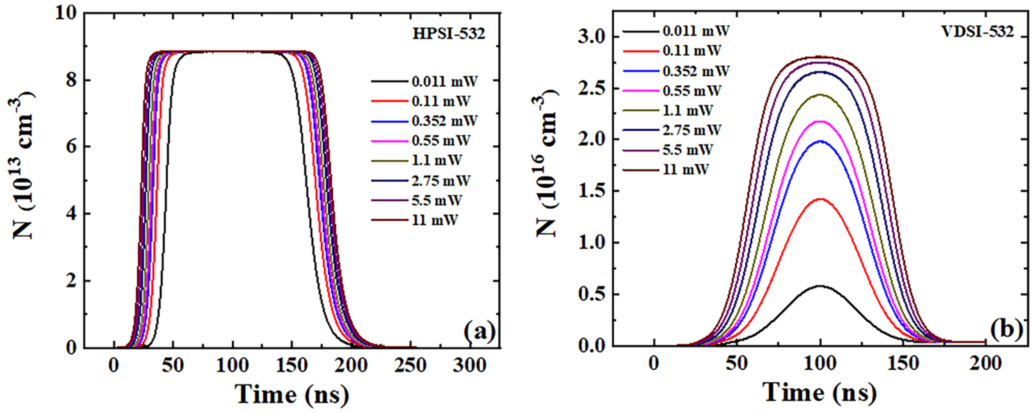

FIG. 5. *N* of HPSI-532 (a) and VDSI-532 (b) with average laser powers.

the dominating recombination mechanism be changed at different laser powers. The impact of lattice temperature on carrier concentration can be ignored because the lattice temperatures add only 11 K at 41 mW for these two samples.

On the one hand, carrier concentration n extracted from the Raman line shape analysis of the LOPC mode is regarded as the average carrier concentration based on the understanding of the primary principles of Raman spectra; on the other hand, the theoretical mean value of the photoexcited carrier concentration (N_{ave}) is obtained by integrating over N calculated from Eqs. (13) and (14). In the numerical calculation, C_{TA} is an adjustable parameter to achieve the goal that N_{ave} is equal to n, as shown in Figs. 6(c) and 6(d). It is found from Fig. 6(e) that the C_{TA} values of these two samples have a linear relationship with the laser power, and they increase to 2.51×10^{-25} for VDSI-355 and 5.98×10^{-25} cm^6/s for HPSI-355 at 41 mW, respectively.

In order to study the photoexcited carrier dynamic, it is necessary to determine which recombination mechanism plays a leading role under different conditions of power laser irradiation. First, the HPSI-355 sample is analyzed. As shown in Fig. 7(a), if *BBA recombination or ambipolar diffusion* (D) *is ignored*, the value of N_{ave} with laser power will hardly change, indicating that their roles are basically negligible. As for the role of *SRH recombination*, the tendencies of N_{ave} with and without SRH vs laser power are essentially the same, but N_{ave} with SRH is slightly lower than that without SRH, indicating that SRH plays a secondary role. *Ignoring TAA recombination*, the N_{ave} value increases nonlinearly with power to 7.7×10^{18} cm^{-3} when the laser power is less than 10 mW. A further increase in power leads to the formation of a linear relationship between N_{ave} and power. N_{ave} at 41 mW can reach 1.8×10^{19} cm^{-3}. At any laser power, N_{ave} without TTA is much larger than that with TTA. Therefore, TAA

TABLE VI. Important parameters for calculation in Eqs. (13)–(16).

Parameters	Value	Reference
D'	$\frac{k_B T}{q}\frac{6.825\times10^{12}}{1.05\times10^{6}\left[\exp\left(\frac{1.92\times10^{-20}}{k_B T}\right)-1\right]+6.5\times10^{6}T^{1.5}}\left[\left(1+\frac{135N}{10^{18}T^{\left(1.3-\frac{18}{T}\right)}}\right)^{2/3}-\frac{113}{T}\left(\frac{N}{10^{18}}\right)^{1/3}\right]$ cm^2/s	49
E_g	$5.26\times10^{-19}-5.60\times10^{-23}\times\frac{T^2}{T+1100}$ J	50
B	1.5×10^{-12} cm^3/s	51
γ_0	$\left(7\times10^{-31}+\frac{3.5\times10^{-9}}{N\times T^{2/3}}\right)\left(1+\frac{N}{7.8\times10^{16}\times T}\right)^{-2}$ cm^6/s	49
D_{L}	$0.1895+8.07\times e^{-T/144}$ cm^2/s	52
C	$2.04+0.12\times e^{-T/288}$ J/K · cm^3	
η	0.008	53
R	0.23	
α (at 355 nm)	$134-0.4T+2.14\times10^{-3}T^2$ cm^{-1}	50
d	1.083×10^{-4} cm	
t_p	20 ns	
$\hbar\omega$	3.495 eV	
k_B	1.38×10^{-23} J/K	

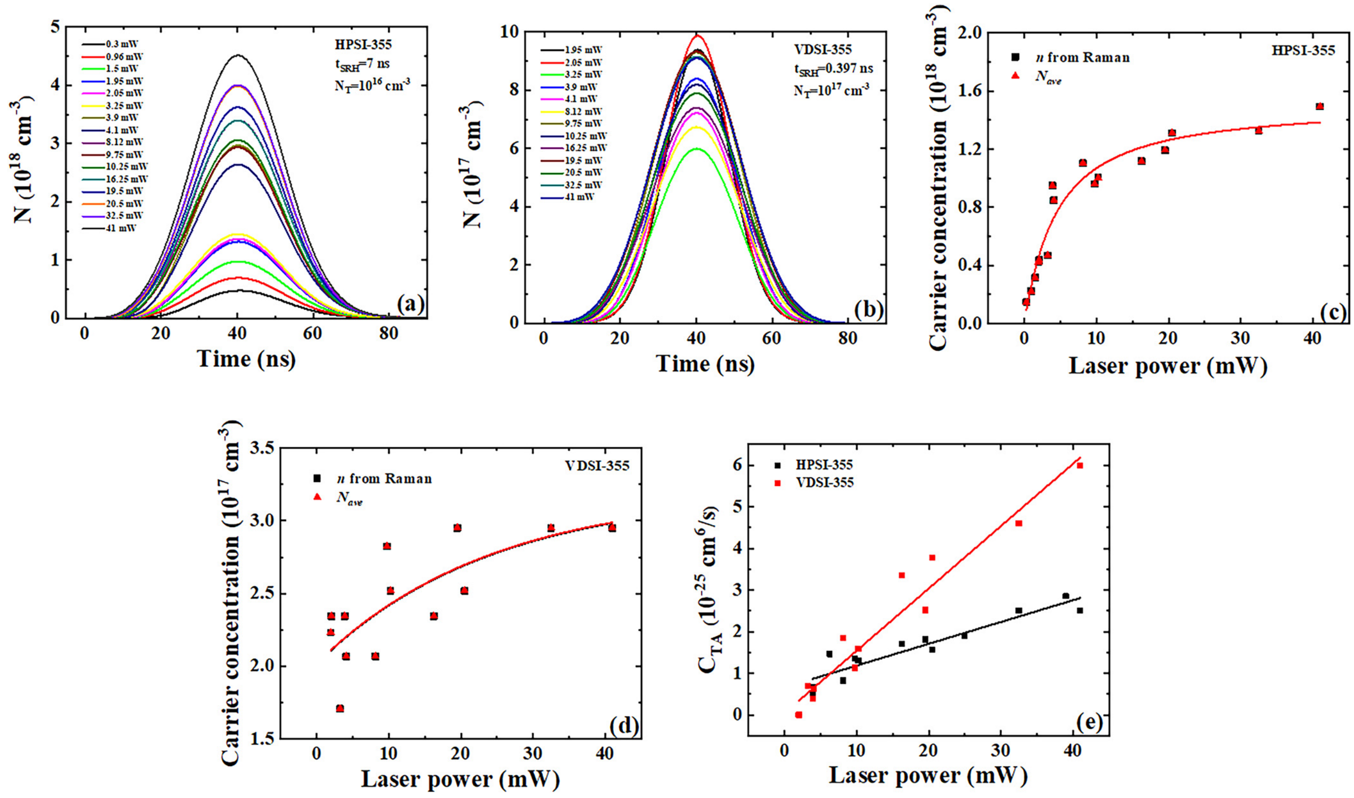

FIG. 6. (a) and (b) N of HPSI-355 and VDSI-355 vs laser power, respectively, (c) and (d) comparison of n and N_{ave} of HPSI-355 and VDSI-355 vs laser power, respectively, and (e) C_{TA} of HPSI-355 and VDSI-355 vs laser power. For modeling, the parameters t_{SRH} and N_T are used: 7 ns from Ref. 9 and 10^{16} cm^{-3} for HPSI, 0.397 ns from Ref. 48, and 10^{17} cm^{-3} for VDSI.

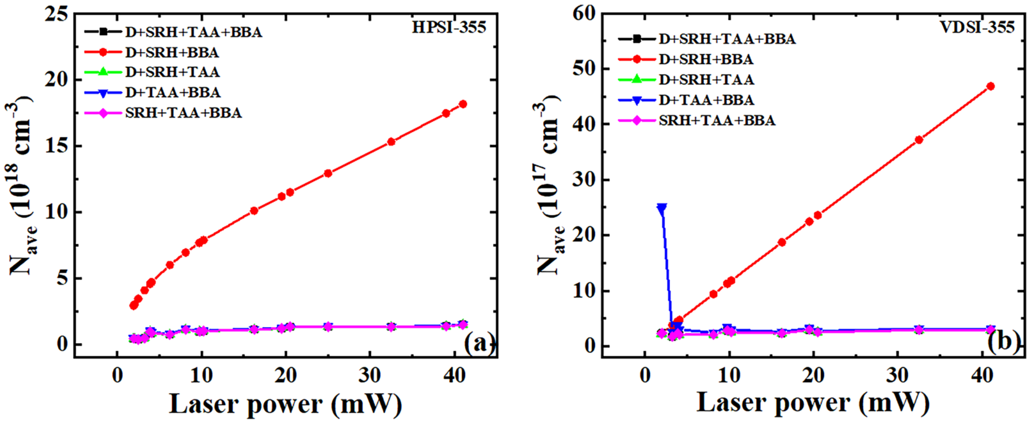

FIG. 7. N_{ave} of HPSI-355 (a) and VDSI-355 (b) with laser powers under four kinds of mechanisms. D, SRH, TAA, and BBA represent ambipolar diffusion, SRH recombination, trap-assisted Auger recombination, and band–band Auger recombination of photoexcited carriers, respectively.

recombination dominates in the recombination process. We can reasonably conclude that the influence of various recombination mechanisms in HPSI decreases in the order of TAA, SRH, and BBA (D). The same method is also adopted for VDSI and the simulation results are illustrated in Fig. 7(b). Like HPSI-355, the effect of BBA and ambipolar diffusion (D) can be ignored. Under low power (<2 mW) irradiation, SRH plays a major role and TAA plays a secondary role. By increasing the laser power, the influence of SRH on N_{ave} plummets, while the impact of TTA increases sharply.

When the 532- nm laser irradiates semi-insulating 4H-SiC substrates, electrons on the partial defect level in the forbidden band are excited to the conduction band due to the fact that the laser photon energy is lower than the bandgap of 4H-SiC (called extrinsic excitation). In consideration of the limitation of trap concentration and carrier recombination, the photogenerated carriers generated by extrinsic excitation during laser irradiation are so low that there is no sufficiently high carrier concentration to be coupled with LO phonons. Therefore, it is difficult to observe the LOPC peak in Raman spectra. This explains why the frequency of LO mode does not vary with the laser power. For 355- nm laser irradiation, the LOPC modes of HPSI and VDSI nonlinearly shift to a high-frequency side with the increase in the laser power and gradually tend to saturation, which reflects exactly in the photogenerated carriers under intrinsic excitation. Numerical results show that this phenomenon is attributed to TAA recombination. SRH recombination is the process involving multi-phonon and/or cascade-phonon emissions, whereas TAA recombination involves secondary electron excitation. Which recombination mechanism is dominant in the defect level in the bandgap depends on the magnitude of $1/t_{SRH}$ and $1/(C_{TA}N_TN)$. If $1/t_{SRH} < 1/(C_{TA}N_TN)$, TAA recombination plays an important role as in the cases of the HPSI and VDSI samples irradiated at high laser powers. Conversely, SRH recombination is significant, as can be demonstrated by VDSI at low laser powers. In this contribution, two phenomena of C_{TA} are worth noting. On the one hand, different doping types have different values of C_{TA}; i.e., the C_{TA} of VDSI is larger than that of HPSI at high laser powers, which is because the position of the VA ($E_c - 0.8$ eV) level is lower than that of the ET ($E_c - 0.55$ eV) and RC ($E_c - 0.63$ eV) levels in HPSI. This explains that the LOPC mode of VDSI saturates earlier than that of HPSI. However, the C_{TA} of VDSI is less than that of HPSI when the laser power is low. We cannot yet give the reason for this phenomenon. On the other hand, C_{TA} increases with the laser power. Taking VDSI-355 as an example, the value of C_{TA} is 4.3×10^{-28} cm^6/s at a lower laser power, which is close to the theoretical value (7.4×10^{-28} cm^6/s) calculated from the formulas in Ref. 54. C_{TA} can increase to the order of 10^{-25} with increasing the laser power. This is due to the fact that the higher the laser power, the higher the photoexcited carrier concentration, the higher the dielectric constant of the semiconductor in the irradiated area, and the higher the transition coefficient of TAA recombination. Therefore, the discovery of TAA recombination on semi-insulating SiC gives us a new insight into carrier recombination.

IV. CONCLUSIONS

The kinetic mechanism of photogenerated carriers of high-purity and vanadium-doped semi-insulating 4H-SiC was investigated by Raman spectra with different laser wavelengths. There is no shift of the longitudinal optical peaks of high-purity and vanadium-doped semi-insulating 4H-SiC with laser power when using a 532- nm laser, whereas there is a nonlinear shift of the longitudinal optical phonon–plasma coupled peaks irradiated by a 355- nm laser to the high-frequency side, and they tend to saturate at high power. The results show that the former is due to a lower photoexcited carrier concentration, while the origin of the latter is complicated. The photogenerated carriers of high-purity semi-insulating 4H-SiC are dominated by trap-assisted Auger recombination, while the influence of Shockley–Read–Hall recombination is extremely limited. The recombination mechanism of vanadium-doped semi-insulating 4H-SiC at different laser powers is different. Shockley–Read–Hall recombination at low laser powers plays an important role, while trap-assisted Auger recombination dominates at high laser powers. The trap-assisted Auger recombination coefficient C_{TA} depends on laser power and the semi-insulating type of the SiC crystal.

In our future work, we will make an attempt to account for some interesting experimental phenomena in photoconductive switches such as the nonlinear increase of its peak current with laser energy and will continue to explore other factors that affect the C_{TA} coefficient to solve the problem left over in this paper. Relevant studies are under way.

ACKNOWLEDGMENTS

This work was supported by the Joint Fund of the National Natural Science Foundation of China (NNSFC) and the China Academy of Physics (NASF) under Grant No. U1830114.

AUTHOR DECLARATIONS

Conflict of Interest

The authors have no conflicts to disclose.

Author Contributions

Meng-meng Gao: Investigation (lead); Writing – original draft (lead). **Liu-yan Fan:** Investigation (equal); Project administration (equal); Supervision (equal); Writing – review & editing (equal). **Xiao-ye Gong:** Investigation (equal); Resources (equal). **Jing-lin You:** Resources (equal). **Zhi-zhan Chen:** Project administration (equal); Resources (equal); Supervision (equal); Writing – review & editing (equal).

DATA AVAILABILITY

The data that support the findings of this study are available within the article.

REFERENCES

[1] E. Janzén, N. T. Son, B. Magnusson, and A. Ellison, Microelectron. Eng. **83**(1), 130 (2006).
[2] N. T. Son, P. Carlsson, A. Gaellstroem, B. Magnusson, and E. Janzen, Appl. Phys. Lett. **91**, 202111 (2007).
[3] A. Ellison, B. Magnusson, N. T. Son, L. Storasta, and E. Janzén, Mater. Sci. Forum **433–436**, 33 (2003).
[4] M. E. Zvanut, V. V. Konovalov, H. Wang, W. C. Mitchel, W. D. Mitchell, and G. Landis, J. Appl. Phys. **96**(10), 5484 (2004).

[5] D. Mauch, W. Sullivan, A. Bullick, A. Neuber, and J. Dickens, IEEE Trans. Plasma Sci. **43**(6), 2021 (2015).

[6] K. Kelkar, C. Fessler, W. C. Nunnally, and N. E. Islam, "Experimental and simulation characterization of semi-insulating 6H SIC photoconductive switch for pulsed power applications," in *2005 IEEE Pulsed Power Conference* (IEEE, 2005), p. 904.

[7] K. Jarašiūnas, P. Ščajev, V. Gudelis, P. B. Klein, and M. Kato, Mater. Sci. Forum **645–648**, 215 (2010).

[8] R. J. Kumar, J. M. Borrego, R. J. Gutmann, J. R. Jenny, D. P. Malta, H. M. Hobgood, and C. H. Carter, Jr, J. Appl. Phys. **102**(1), 013704 (2007).

[9] L. Storasta, R. Aleksiejūnas, M. Sūdžius, A. Kadys, T. Malinauskas, K. Jarašiūnas, B. Magnusson, and E. Janzén, Mater. Sci. Forum **483–485**, 409 (2005).

[10] T. Malinauskas, "Investigation of carrier dynamics in wide bandgap semiconductors by light-induced transient grating technique," Ph.D. thesis (Vilniaus Universitetas, 2009).

[11] P. T. Landsberg, Phys. Status Solidi B **41**(2), 457 (1970).

[12] A. Hangleiter, Phys. Rev. B: Condens. Matter Mater. Phys. **35**(17), 9149 (1987).

[13] J. P. Ma, Z. M. Chen, G. Lu, L. M. Hang, X. F. Feng, and T. M. Lei, Chin. Phys. Lett. **18**(8), 1123 (2001).

[14] J. L. You, G. C. Jiang, H. Y. Hou, Y. Q. Wu, and K. D. Xu, Chin. Phys. Lett. **19**(2), 205 (2002).

[15] X. B. Li, Z. Z. Chen, and E. W. Shi, Physica B **405**(10), 2423 (2010).

[16] M. V. Klein, B. N. Ganguly, and P. J. Colwell, Phys. Rev. B **6**(6), 2380 (1972).

[17] S. Nakashima, H. Harima, T. Tomita, and T. Suemoto, Phys. Rev. B **62**(24), 16605 (2000).

[18] H. Harima, T. Hosoda, and S. Nakashima, Mater. Sci. Forum **338–342**, 607 (2000).

[19] S. Nakashima, T. Kitamura, T. Mitani, H. Okumura, M. Katsuno, and N. Ohtani, Phys. Rev. B **76**(24), 4692 (2007).

[20] H. Y. Sun, S. C. Lien, Z. R. Qiu, H. C. Wang, T. Mei, C. W. Liu, and Z. C. Feng, Opt. Express **21**(22), 26475 (2013).

[21] M. Bauer, A. M. Gigler, A. J. Huber, R. Hillenbrand, and R. W. Stark, J. Raman Spectrosc. **40**(12), 1867 (2009).

[22] N. Piluso, A. Severino, M. Camarda, R. Anzalone, A. Canino, G. Condorelli, G. Abbondanza, and F. La Via, Mater. Sci. Forum **645–648**, 255 (2010).

[23] T. Liu, Z. W. Xu, M. Rommel, H. Wang, Y. Song, Y. F. Wang, and F. Z. Fang, Crystal **9**(8), 428 (2019).

[24] J. C. Burton, L. Sun, M. Pophristic, S. J. Lukacs, F. H. Long, Z. C. Feng, and I. T. Ferguson, J. Appl. Phys. **84**(11), 6268 (1998).

[25] D. T. Hon and W. L. Faust, Appl. Phys. **1**(5), 241 (1973).

[26] M. V. Klein, *Light Scattering in Solids* (Springer, Berlin, 1975).

[27] G. Irmer, V. V. Toporov, B. H. Bairamov, and J. Monecke, Phys. Status Solidi B **119**(2), 595 (1983).

[28] S. Nakashima, Y. Nakatake, Y. Ishida, T. Takahashi, and H. Okumura, Mater. Sci. Forum **389–393**, 629 (2002).

[29] H. Yugami, S. Nakashima, A. Mitsuishi, A. Uemoto, M. Shigeta, K. Furukawa, A. Suzuki, and S. Nakajima, J. Appl. Phys. **61**(1), 354 (1987).

[30] H. Harima, S. I. Nakashima, and T. Uemura, J. Appl. Phys. **78**(3), 1996 (1995).

[31] S. Nakashima, T. Kitamura, T. Kato, K. Kojima, R. Kosugi, H. Okumura, H. Tsuchida, and M. Ito, Appl. Phys. Lett. **93**(12), 121913 (2008).

[32] C. Kittel, *Introduction to Solid State Physics*, 8th ed. (John Wiely & Sons, Inc., 2005).

[33] Z. Y. Feng, L. F. Xiao, C. B. Luan, Y. F. Li, H. R. Sha, H. T. Li, and X. G. Xu, Appl. Opt. **60**(11), 3182 (2021).

[34] W. Götz, A. Schöner, G. Pensl, W. Suttrop, W. J. Choyke, R. Stein, and S. Leibenzeder, J. Appl. Phys. **73**(7), 3332 (1993).

[35] M. Suproniuk, M. Wierzbowski, and P. Paziewski, Sci. Rep. **10**(1), 11865 (2020).

[36] W. C. Mitchel, W. D. Mitchell, S. R. Smith, G. R. Landis, A. O. Evwaraye, Z. Q. Fang, D. C. Look, and J. R. Sizelove, Mater. Sci. Forum **527–529**, 505 (2006).

[37] P. B. Klein, J. Appl. Phys. **103**, 033702 (2008).

[38] M. E. Zvanut and V. V. Konovalov, Appl. Phys. Lett. **80**(3), 410 (2002).

[39] M. Suproniuk, P. Kamiński, R. Kozłowski, M. Pawłowski, and M. Wierzbowski, Opto-Electron. Rev. **25**(3), 171 (2017).

[40] J. R. Jenny, J. Skowronski, W. C. Mitchel, H. M. Hobgood, R. C. Glass, G. Augustine, and R. H. Hopkins, Appl. Phys. Lett. **68**(14), 1963 (1996).

[41] J. S. Sullivan, "Wide bandgap extrinsic photoconductive switches," Ph.D thesis (University of California, 2013).

[42] M. Suproniuk, P. Kamiński, R. Kozłowski, and M. Pawłowski, Acta Phys. Pol. A **125**, 1042 (2014).

[43] S. Sasaki, K. Kawahara, G. Feng, G. Alfieri, and T. Kimoto, J. Appl. Phys. **109**(1), 013705 (2011).

[44] C. Longneaud, J. Kleider, P. Kaminski, R. Koslowski, and M. Miczuga, J. Phys.: Condens. Matter **21**(4), 045801 (2009).

[45] S. H. Lee, H. S. Sim, J. Lee, J. M. Kim, and Y. E. Shin, Mater. Trans. **47**(11), 2835 (2006).

[46] V. Driel and H. M, Appl. Phys. Lett. **40**(5), 385 (1982).

[47] J. G. Fossum, R. P. Mertens, D. S. Lee, and J. F. Nijs, Solid State Electron. **26**(6), 569 (1983).

[48] G. Tamulaitis, I. Yilmaz, M. S. Shur, T. Anderson, and R. Gaska, Appl. Phys. Lett. **84**(3), 335 (2004).

[49] P. Ščajev and K. Jarašiūnas, J. Phys. D: Appl. Phys. **46**(26), 265304 (2013).

[50] A. Galeckas, P. Grivickas, V. Grivickas, V. Bikbajevas, and J. Linnros, Phys. Status Solidi A **191**(2), 613 (2002).

[51] P. Ščajev, V. Gudelis, K. Jarašiūnas, and P. B. Klein, J. Appl. Phys. **108**, 023705 (2010).

[52] R. S. Wei, S. Song, K. Yang, Y. X. Cui, Y. Peng, X. F. Chen, X. B. Hu, and X. G. Xu, J. Appl. Phys. **113**(5), 053503 (2013).

[53] T. V. Blank, Y. A. Gol'dberg, E. V. Kalinina, O. V. Konstantinov, A. O. Konstantinov, and A. Hallen, Tech. Phys. Lett. **27**(9), 776 (2001).

[54] F. Staub, U. Rau, and T. Kirchartz, ACS Omega **3**(7), 8009 (2018).